Table 4.3.4.2. *Plasmon energies measured (and calculated) for a few simple metals; most data have been extracted from Raether (1980)*

Monovalent			Divalent			Trivalent			Tetravalent		
$\hbar\omega_p$ (eV)			$\hbar\omega_p$ (eV)			$\hbar\omega_p$ (eV)			$\hbar\omega_p$ (eV)		
	Meas.	Calc.		Meas.	Calc.		Meas.	Calc.		Meas.	Calc.
Li	7.1	(8.0)	Be	18.7	(18.4)	B	22.7	(?)	C	34.0	(31)
Na	5.7	(5.9)	Mg	10.4	(10.9)	Al	14.95	(15.8)	Si	16.5	(16.6)
K	3.7	(4.3)	Ca	8.8	(8.0)	Ga	13.8	(14.5)	Ge	16.0	(15.6)
Rb	3.4	(3.9)	Sr	8.0	(7.0)	In	11.4	(12.5)	Sn	13.7	(14.3)
Cs	2.9	(3.4)	Ba	7.2	(6.7)	Sc	14.0	(12.9)	Pb	(13)	(13.5)

solution, reproduced in Fig. 4.3.4.11, is due to Castaing & Henry (1962). It consists of a double magnetic prism and a concave electrostatic mirror biased at the potential of the microscope cathode. The system possesses two pairs of stigmatic points that may coincide with a diffraction plane and an image plane of the electron-microscope column. One of these sets of points is achromatic and can be used for image filtering. The other is strongly chromatic and is used for spectrum analysis. Zanchi, Sevely & Jouffrey (1977) and Rose & Plies (1974) have proposed replacing this system, which requires an extra source of high voltage for the mirror, by a purely magnetic equivalent device. Several solutions, known as the α and ω filters, with three or four magnets, have thus been built, both on very high voltage microscopes (Zanchi, Perez & Sevely, 1975) and on more conventional ones (Krahl & Herrmann, 1980), the latest version now being available from one EM manufacturer (Zeiss EM S12).

4.3.4.2.3. *Detection systems*

The final important component in EELS is the detector that measures the electron flux in the dispersion plane of the spectrometer and transfers it through a suitable interface to the data storage device for further computer processing. Until about 1990, all systems were operated in a sequential acquisition mode. The dispersed beam was scanned in front of a narrow slit located in the spectrometer dispersion plane. Electrons were then generally recorded by a combination of scintillator and photomultiplier capable of single electron counting.

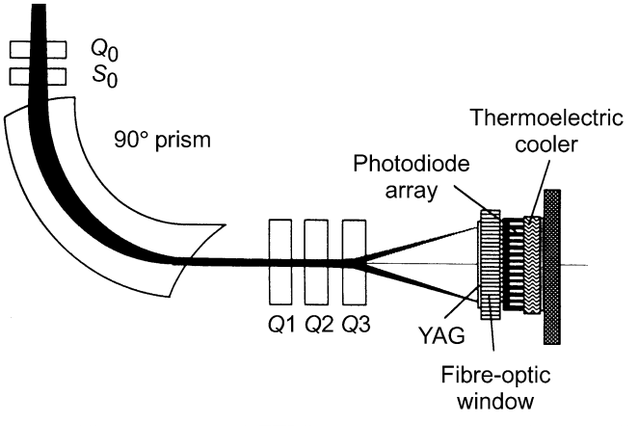

Fig. 4.3.4.12. A commercial EELS spectrometer designed for parallel detection on a photodiode array. The family of quadrupoles controls the dispersion on the detector level [courtesy of Krivanek *et al.* (1987))].

This process is, however, highly inefficient: while the counts are measured in one channel, all information concerning the other channels is lost. These requirements for improved detection efficiency have led to the consideration of possible solutions for parallel detection of the EELS spectrum. They use a multiarray of detectors, the position, the size and the number of which have to be adapted to the spectral distribution delivered by the spectrometer. In most cases with magnetic type devices, auxiliary electron optics has to be introduced between the spectrometer and the detector so that the dispersion matches the size of the individual detection cells. Different systems have been proposed and tested for recording media, the most widely used solutions at present being the photodiode and the charge-coupled diode arrays described by Shuman & Kruit (1985), Krivanek, Ahn & Keeney (1987), Strauss, Naday, Sherman & Zaluzec (1987), Egerton & Crozier (1987), Berger & McMullan (1989), *etc.* Fig. 4.3.4.12 shows a device, now commercially available from Gatan, that is made of a convenient combination of these different components. This progress in detection has led to significant improvements in many areas of EELS: enhanced detection limits, reduced beam damage in sensitive materials, data of improved quality in terms of both SNR and resolution, and access to time-resolved spectroscopy at the ms time scale (chronospectra). Several of these important consequences are illustrated in the following sections.

4.3.4.3. *Excitation spectrum of valence electrons*

Most inelastic interaction of fast incident electrons is with outer atomic shells in atoms, or in solids with valence electrons (referred to as conduction electrons in metals). These involve excitations in the 0–50 eV range, but, in a few cases, interband transitions from low-binding-energy shells may also contribute.

4.3.4.3.1. *Volume plasmons*

The basic concept introduced by the many-body theory in the interacting free electron gas is the volume plasmon. In a condensed material, the assembly of loosely bound electrons behaves as a plasma in which collective oscillations can be induced by a fast external charged particle. These eigenmodes, known as *volume plasmons*, are longitudinal charge-density fluctuations around the average bulk density in the plasma $n \simeq 10^{28}$ e$^-$/m^3). Their eigen frequency is given, in the free electron gas, as

$$\omega_p = \left(\frac{n e^2}{m\varepsilon_0}\right)^{1/2}. \qquad (4.3.4.8)$$

The corresponding $\hbar\omega_p$ energy, measured in an energy-loss spectrum (see the famous example of the plasmon in aluminium

Table 4.3.4.3. *Experimental and theoretical values for the coefficient α in the plasmon dispersion curve together with estimates of the cut-off wavevector (from Raether, 1980)*

	Measured α	Calculated α	q_c (Å^{-1})
Li	0.24	0.35	0.9
Na	0.24	0.32	0.8
K	0.14	0.29	0.8
Mg	0.35	0.39	1.0
Al	0.2 (<0.5 Å^{-1})		
	0.45 (>0.5 Å^{-1})	0.43	1.3
In	0.40 (<0.5 Å^{-1})		
	0.66 (>0.5 Å^{-1})		
Si	0.41		
	0.3	0.45	1.1

Table 4.3.4.4. *Comparison of measured and calculated values for the halfwidth $\Delta E_{1/2}(0)$ of the plasmon line (from Raether, 1980)*

	Experimental (eV)	Theory (eV)
Li	2.2	2.55
Na	0.3	0.12
K	0.25	0.15
Rb	0.6	0.64
Cs	1.2	0.96
Al	0.53	0.43
Mg	0.7	0.7
Si	3.2	5.4
Ge	3.1	3.9

in Fig. 4.3.4.3), is the *plasmon energy*, for which typical values in a selection of pure solid elements are gathered in Table 4.3.4.2. The accuracies of the measured values depend on several instrumental parameters. Moreover, they are sensitive to the specimen crystalline state and to its degree of purity. Consequently, there exist slight discrepancies between published values. Numbers listed in Table 4.3.4.2 must therefore be accepted with a 0.1 eV confidence. Some specific cases require comments: amorphous boron, when prepared by vacuum evaporation, is not a well defined specimen. Carbon exists in several allotropic varieties. The selection of the diamond type in the table is made for direct comparison with the other tetravalent specimens (Si, Ge, Sn). The results for lead (Pb) are still subject to confirmation. The volumic mass density is an important factor (through n) in governing the value of the plasmon energy. It varies with temperature and may be different in the crystal, in the amorphous, and in the liquid phases. In simple metals, the amorphous state is generally less dense than the crystalline one, so that its plasmon energy shifts to lower energies.

The above description applies only to very small scattering vectors $\mathbf{q}$. In fact, the plasmon energy increases with scattering angle (and with momentum transfer $\hbar\mathbf{q}$). This dependence is known as the dispersion relation, in which two distinct behaviours can be described:

(a) For small momentum transfers ($q \lesssim q_c$), the dispersion curve is parabolic:

$$\hbar\omega_p(q) = \hbar\omega_p(0) + \frac{\alpha\hbar^2}{m_0} q^2. \qquad (4.3.4.9)$$

The coefficient α has been measured in a number of substances and calculated for the free-electron case in the random phase approximation (Lindhard, 1954); see Table 4.3.4.3 for some data. A simple expression for α is

$$\alpha = \tfrac{3}{5}\frac{E_F}{\hbar\omega_p(0)}, \qquad (4.3.4.10)$$

where E_F is the Fermi energy of the electron gas. More detailed observations indicated that it is not possible to describe the dispersion curve over a large momentum range with a single q^2 law. In fact, one has to fit the experiment data with different linear or quadratic slopes as a function of q [see values indicated for Al and In in Table 4.3.4.3, and Hohberger, Otto & Petri (1975)]. Moreover, anisotropy has been found along different $\mathbf{q}$ directions in monocrystals (Manzke, 1980). In parallel, refinements have been brought into the calculations by including band-structure effects to deal with the anisotropy of the dispersion relation and with the bending of the experimental curves. Electron–electron correlations have also been considered, which has slightly improved the agreement between calculated and measured values of α (Bross, 1978*a*, *b*).

(b) For large momentum transfers, there exists a critical wavevector q_c, which corresponds to a strong decay of the plasmon mode into single electron–hole pair excitations. This can be calculated using conservation rules in energy and momentum, giving

$$\hbar\omega_p(0) + \alpha\frac{\hbar^2}{m_0} q_c^2 = \frac{\hbar^2}{2m_0}(q_c^2 + 2q_c q_F), \qquad (4.3.4.11)$$

where q_F is the Fermi wavevector. A simple approximation is $q_c \simeq \omega_p/v_F$, v_F being the Fermi velocity. Single pair excitations can be created by fast incoming electrons in the domain of scattering conditions contained between the two curves:

$$\left.\begin{aligned} \Delta E_{\max} &= \frac{\hbar^2}{2m_0}(q^2 + 2qq_F) \\ \Delta E_{\min} &= \frac{\hbar^2}{2m_0}(q^2 - 2qq_F) \end{aligned}\right\} \qquad (4.3.4.12)$$

shown in Fig. 4.3.4.13. They bracket the curve $\Delta E = \hbar^2 q^2/2m_0$ corresponding to the transfer of energy and momentum to an isolated free electron. For momentum transfers such as $q > q_c$, the plasmon mode is heavily damped and it is difficult to distinguish its own specific behaviour from the electron–hole continuum. A few studies, *e.g.* Batson & Silcox (1983), indicate that the plasmon dispersion curve flattens as it enters the

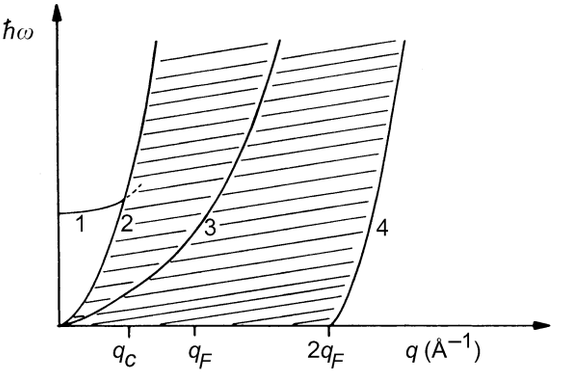

Fig. 4.3.4.13. The dispersion curve for the excitation of a plasmon (curve 1) merges into the continuum of individual electron–hole excitations (between curves 2 and 4) for a critical wavevector q_c. The intermediate curve (3) corresponds to Compton scattering on a free electron.

quasiparticle domain and approaches the centre of the continuum close to the free-electron curve. However, not only is the scatter between measurements fairly high, but a satisfactory theory is not yet available [see Schattschneider (1989) for a compilation of data on the subject].

Plasmon lifetime is inversely proportional to the energy width of the plasmon peak $\Delta E_{1/2}$. Even for Al, with one of the smallest plasmon energy widths ($\simeq 0.5$ eV), the lifetime is very short: after about five oscillations, their amplitude is reduced to $1/e$. Such a damping demonstrates the strength of the coupling of the collective modes with other processes. Several mechanisms compete for plasmon decay:

(*a*) For small momentum transfer, it is generally attributed to vertical interband transitions. Table 4.3.4.4, extracted from Raether (1980), compares a few measured values of $\Delta E_{1/2}(0)$, with values calculated using band-structure descriptions.

(*b*) For moderate momentum transfer q, a variation law such as

$$\Delta E_{1/2}(q) = \Delta E_{1/2}(0) + Bq^2 + O(q^4) \qquad (4.3.4.13)$$

has been measured. The q dependence of $\Delta E_{1/2}$ is mainly accounted for by non-vertical transitions compatible with the band structure, the number of these transitions increasing with q (Sturm, 1982). Other mechanisms have also been suggested, such as phonons, *umklapp* processes, scattering on surfaces, *etc*.

(*c*) For large momentum transfer (*i.e.* of the order of the critical wavevector q_c), the collective modes decay into the strong electron–hole-pair channels already described giving rise to a clear increase of the damping for values of $q > q_c$.

Within this free-electron-gas description, the differential cross section for the excitation of bulk plasmons by incident electrons of velocity v is given by

$$\frac{\mathrm{d}\sigma_p}{\mathrm{d}\Omega}(\theta) = \frac{\Delta E_p}{2\pi N a_0 m_0 v^2} \frac{1}{\theta^2 + \theta_E^2}, \qquad (4.3.4.14)$$

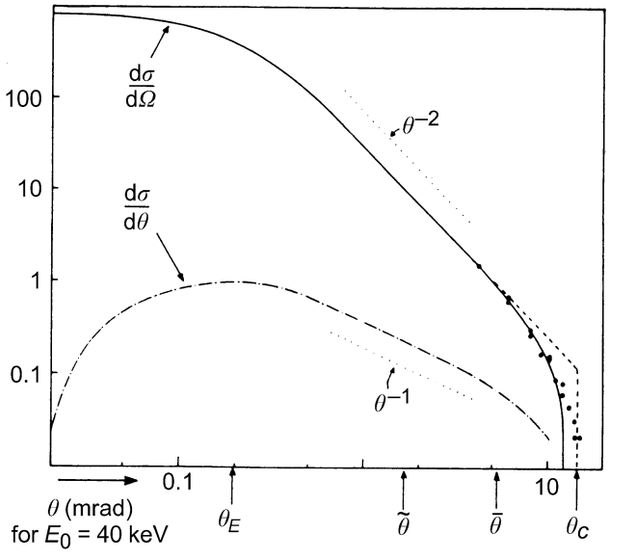

Fig. 4.3.4.14. Measured angular dependence of the differential cross section $\mathrm{d}\sigma/\mathrm{d}\Omega$ for the 15 eV plasmon loss in Al (dots) compared with a calculated curve by Ferrell (solid curve) and with a sharp cut-off approximation at θ_c (dashed curved). Also shown along the scattering angle axis, θ_E = characteristic inelastic angle defined as $\Delta E/2E_0$, $\tilde{\theta}$ = median inelastic angle defined by $\int_0^{\tilde{\theta}} (\mathrm{d}\sigma/\mathrm{d}\Omega)\,\mathrm{d}\Omega = 1/2 \int_0^{\theta_c} (\mathrm{d}\sigma/\mathrm{d}\Omega)\,\mathrm{d}\Omega$, and $\bar{\theta}$ = average inelastic angle defined by $\bar{\theta} = \int \theta(\mathrm{d}\sigma/\mathrm{d}\Omega)\,\mathrm{d}\Omega / \int (\mathrm{d}\sigma/\mathrm{d}\Omega)\,\mathrm{d}\Omega$ [courtesy of Egerton (1986)].

where N is the density of atoms per volume unit and θ_E is the characteristic inelastic angle defined as $\Delta E_p/2E_0$ in the non-relativistic description and as $\Delta E_p/\gamma m_0 v^2$ {with $\gamma = [1 - (v^2/c^2)]^{-1/2}$} in the relativistic case. The angular dependence of the differential cross section for plasmon scattering is shown in Fig. 4.3.4.14. The integral cross section up to an angle β_0 is

$$\sigma_p(\beta_0) = \int_0^{\beta_0} \left(\frac{\mathrm{d}\sigma_p}{\mathrm{d}\Omega}\right) \mathrm{d}\Omega = \frac{\Delta E_p \log(\beta_0/\theta_E)}{N a_0 m_0 v^2}. \qquad (4.3.4.15)$$

The total plasmon cross section is calculated for $\beta_0 = \theta_c = q_c/k_0$. Converted into mean free path, this becomes

$$\Lambda_p = \frac{1}{N\sigma_p} = \frac{a_0}{\theta_E} \left(\log \frac{\theta_c}{\theta_E}\right)^{-1} \quad \text{(non-relativistic formula);} \qquad (4.3.4.16)$$

and

$$\Lambda_p = \frac{a_0 \gamma m_0 v^2}{\Delta E_p} \left(\log \frac{\hbar q_c v}{1.132 \hbar \omega_p}\right)^{-1} \quad \text{(relativistic formula).} \qquad (4.3.4.17)$$

The behaviour of Λ_p as a function of the primary electron energy is shown in Fig. 4.3.4.15.

4.3.4.3.2. *Dielectric description*

The description of the bulk plasmon in the free-electron gas can be extended to any type of condensed material by introducing the dielectric response function $\varepsilon(\mathbf{q}, \omega)$, which describes the frequency and wavevector-dependent polarizability of the medium; *cf*. Daniels *et al* (1970). One associates, respectively, the ε_T and ε_L functions with the propagation of transverse and longitudinal EM modes through matter. In the small-$\mathbf{q}$ limit, these tend towards the same value:

$$\lim_{q\to 0} \varepsilon_T(\mathbf{q}, \omega) = \lim_{q\to 0} \varepsilon_L(\mathbf{q}, \omega) = \varepsilon(0, \omega).$$

As transverse dielectric functions are only used for wavevectors close to zero, the T and L indices can be omitted so that:

$$\varepsilon_L(\mathbf{q}, \omega) = \varepsilon(\mathbf{q}, \omega) \quad \text{and} \quad \varepsilon_T(\mathbf{q}, \omega) = \varepsilon(0, \omega).$$

The transverse solution corresponds to the normal propagation of EM waves in a medium of dielectric coefficient $\varepsilon(0, \omega)$, *i.e.* to

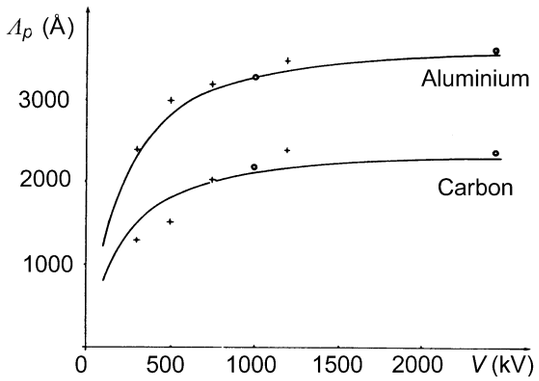

Fig. 4.3.4.15. Variation of plasmon excitation mean free path Λ_p as a function of accelerating voltage V in the case of carbon and aluminium [courtesy of Sevely (1985)].

references